

Real-Time Position-Aware View Synthesis from Single-View Input

MANU GOND, Mid Sweden University, Sweden and Technical University of Berlin, Germany

EMIN ZERMAN, Mid Sweden University, Sweden

SEBASTIAN KNORR, HTW Berlin - University of Applied Sciences, Germany

MÅRTEN SJÖSTRÖM, Mid Sweden University, Sweden

Recent advancements in view synthesis have significantly enhanced immersive experiences across various computer graphics and multimedia applications, including telepresence, and entertainment. By enabling the generation of new perspectives from a single input view, view synthesis allows users to better perceive and interact with their environment. However, many state-of-the-art methods, while achieving high visual quality, face limitations in real-time performance, which makes them less suitable for live applications where low latency is critical. In this paper, we present a lightweight, position-aware network designed for real-time view synthesis from a single input image and a target camera pose. The proposed framework consists of a Position Aware Embedding, modeled with a multi-layer perceptron, which efficiently maps positional information from the target pose to generate high dimensional feature maps. These feature maps, along with the input image, are fed into a Rendering Network that merges features from dual encoder branches to resolve both high level semantics and low level details, producing a realistic new view of the scene. Experimental results demonstrate that our method achieves superior efficiency and visual quality compared to existing approaches, particularly in handling complex translational movements without explicit geometric operations like warping. This work marks a step toward enabling real-time view synthesis from a single image for live and interactive applications.

CCS Concepts: • **Computing methodologies** → *Neural networks; Computer graphics*.

Additional Key Words and Phrases: Light Field, View Synthesis, Deep Learning, Immersive Imaging, Rendering

ACM Reference Format:

Manu Gond, Emin Zerman, Sebastian Knorr, and Mårten Sjöström. 2018. Real-Time Position-Aware View Synthesis from Single-View Input. In *Proceedings of Make sure to enter the correct conference title from your rights confirmation email (Conference acronym 'XX)*. ACM, New York, NY, USA, 13 pages. <https://doi.org/XXXXXXXX.XXXXXXX>

1 Introduction

Telepresence systems [Dima and Sjöström 2021] enable users to interact with remote environments in real time, offering a wide

Authors' Contact Information: Manu Gond, manu.gond@miun.se, Mid Sweden University, Sundsvall, Sweden and Technical University of Berlin, Berlin, Germany; Emin Zerman, emin.zerman@miun.se, Mid Sweden University, Sundsvall, Sweden, emin.zerman@miun.se; Sebastian Knorr, HTW Berlin - University of Applied Sciences, Berlin, Germany; Mårten Sjöström, marten.sjostrom@miun.se, Mid Sweden University, Sundsvall, Sweden.

Permission to make digital or hard copies of all or part of this work for personal or classroom use is granted without fee provided that copies are not made or distributed for profit or commercial advantage and that copies bear this notice and the full citation on the first page. Copyrights for components of this work owned by others than the author(s) must be honored. Abstracting with credit is permitted. To copy otherwise, or republish, to post on servers or to redistribute to lists, requires prior specific permission and/or a fee. Request permissions from permissions@acm.org.

Conference acronym 'XX, June 03–05, 2018, Woodstock, NY

© 2018 Copyright held by the owner/author(s). Publication rights licensed to ACM.

ACM ISBN 978-1-4503-XXXX-X/18/06

<https://doi.org/XXXXXXXX.XXXXXXX>

range of applications, particularly in sectors such as heavy machinery, where remote operation from a safe distance is crucial. These systems have the potential to facilitate seamless natural interaction with remote environments. Current telepresence technologies typically rely on head-mounted displays (HMDs), high-speed networks, and consumer or industrial-grade cameras to deliver live video feeds of the environment. While 2D video feeds provide some pictorial information, the lack of depth perception significantly limits situational awareness, which is vital for effective remote operation.

The challenge to have an understanding of a remote site's structure may be address by enabling motion parallax for the user. I.e., the user moves the head forth and back to get a notion of the scene depth. This requires access to views from different perspectives, where camera positions and poses need to be continuous for a smooth transition and a high quality experience. Therefore, it is imperative to render continuous perspective views accurately and in real time for applications such as augmented reality (AR), virtual reality (VR), and telepresence systems.

The synthesis of views from perspectives continuous in camera position and pose requires sufficient information of the scene. Early methods employed view interpolations and depth-image-based rendering, but both these require multiple capture devices resulting in calibration issues and high communication capacity requirements. Therefore, generating new views from a single input image and a specified camera pose has emerged as a key task in rendering. A variety of approaches, such as Neural Radiance Fields (NeRF) [Mildenhall et al. 2021] and more recent transformer-based architectures like NViST [Jang and Agapito 2024], have been proposed to tackle this problem. These methods leverage both synthetic and real-world datasets to produce high-quality novel views. However, most state-of-the-art methods either require multi-view inputs or are computationally intensive, making them unsuitable for real-time applications where low latency is critical.

In this work, we build upon the growing body of research on single-image-based view synthesis. We introduce a learning based position embedding method combined with a rendering network that efficiently synthesizes high-quality views of arbitrary camera location and pose using fewer computational resources. Our method maintains high fidelity even when handling large translational shifts, making it ideal for real-time applications and practical deployment on consumer devices. To train and test our method we also create our own synthetic dataset using Blender.

Unlike other methods, such as NViST, which employs transformer architectures, or SE3D [Koh et al. 2023], which utilizes large-scale generative-adversarial networks (GANs) to address occlusions and complex scenes, our network is designed to be lightweight and computationally efficient. Despite its smaller footprint, it excels in handling scenarios where translational movements dominate,

enabling real-time inference. In summary, our main contributions are as follows:

- A lightweight network with a positional embedding module that can generate novel views within a given baseline without requiring explicit operations.
- A positional encoding scheme similar to NeRF, which is combined with a multi-layer perceptron (MLP), to create a more generalizable framework capable of handling different scenes.
- Our method achieves real-time performance, with inference times of approximately 8.6 milliseconds, corresponding to over 100 frames per second (FPS) for images at a resolution of 512x512 pixels.

The remainder of this paper is organized as follows: Section 2 reviews state-of-the-art methods aimed at view synthesis. Section 3, and 4 describes the proposed approach for small baseline and large baseline rendering. Section 5 provides a comparative analysis of the results, including quality and speed evaluations. Finally, conclusions are summarized in Section 7.

2 Background

View synthesis has recently become a pivotal research area in immersive telepresence, aiming to generate unseen perspectives of a remote scene from a limited set of input images. Traditional approaches, such as structure-from-motion (SfM) and multi-view stereo (MVS), rely on geometric consistency between input views to reconstruct novel viewpoints [Seitz and Dyer 1999]. While these methods have shown effectiveness in controlled environments, their performance deteriorates in complex real-world scenarios and often necessitates multiple input views to achieve high-quality results. In light of these limitations, more recent methods focus on synthesizing novel views from a sparse or single image. This section outlines these advancements and their respective contributions to the field of view synthesis.

2.1 Scene Regression Approaches

Recent advancements in view synthesis have centered around methods that aim to represent a scene from sparse image inputs, particularly those leveraging neural implicit representations such as NeRF [Mildenhall et al. 2021]. A NeRF encodes a scene as a continuous volumetric function, allowing novel view generation through volumetric rendering. Despite its capacity to produce highly photorealistic images, NeRF suffers from computational inefficiencies, particularly in terms of inference time. Several techniques have been proposed to mitigate these limitations, such as hash encoding in InstantNGP [Müller et al. 2022] and multi-scale representations in Mip-NeRF [Barron et al. 2021]. While these improvements accelerate rendering, they retain significant reliance on MLPs, which remain computationally expensive.

To address these concerns, methods like Plenoxels [Fridovich-Keil et al. 2022] have emerged, leveraging spherical harmonics to represent a scene without the need for deep neural networks. Though Plenoxels achieves faster optimization than many NeRF-based methods, it still falls short in terms of memory efficiency. A more recent innovation, Gaussian Splatting [Kerbl et al. 2023], improves memory and rendering efficiency by employing high-dimensional Gaussian

kernels to represent the scene. However, its optimal performance still depends on the availability of multiple input views.

2.2 Light Field Reconstruction and Rendering

Light field (LF) representation encodes both the spatial and angular information of a scene, often described by an $H \times W \times N \times N$ structure, where $H \times W$ refers to the spatial resolution and $N \times N$ denotes the angular resolution [Levoy and Hanrahan 1996]. This representation facilitates tasks like viewpoint manipulation [Zhou et al. 2020]. LF reconstruction methods aim to generate a dense $N \times N$ light field from a single input view or a few input views, eliminating the need for complex multi-camera setups.

A common LF reconstruction approach utilizes convolutional neural networks (CNNs) to estimate scene depth [Srinivasan et al. 2017], followed by warping operators to generate target views. To address warping artifacts, subsequent refinement networks have been developed [Zhou et al. 2020, 2021]. Other methods exploit depth estimation or optical flow [Cun et al. 2019], appearance flow [Ivan et al. 2019], or a combination of both [Bae et al. 2021] to synthesize the light field.

In more recent developments, GANs [Chandramouli et al. 2020; Chen et al. 2020] and auto-encoders [Han and Xiang 2022] have demonstrated effectiveness in reconstructing dense light fields from a single image input. Additionally, LFSphereNet [Gond et al. 2023] extends LF reconstruction to spherical light fields using a single omnidirectional image. Furthermore, to generate the novel views from the LFs, the algorithms like dynamically reparameterized LFs [Isaksen et al. 2000] and per-view disk-based blending [Overbeck et al. 2018] have to be utilized which have higher memory footprint, making the whole process unsuitable for dynamic environments and low memory systems.

Our proposed method, PLFNet (described in Sec 3), contributes to LF reconstruction and rendering by directly synthesizing views within a local LF volume, thus eliminating the need of additional rendering algorithms.

2.3 Learning-Based Approaches

Learning-based methods seek to overcome the limitations of both scene regression and light field rendering approaches, which include constraints such as low baselines, sparse image input requirements, and slow rendering times. Several models, including PixelNeRF [Yu et al. 2021] and VisionNeRF [Lin et al. 2023], have been developed to generalize NeRF to novel scenes by conditioning the network on image features. Despite their promise, these methods often face challenges such as scale ambiguity and difficulty in handling large translational movements.

To address these challenges, the diffusion model based approach in 3DiM [Watson et al. 2022] employs pose guided diffusion to improve performance, particularly in scenarios with large translational movement. Fine-tuning diffusion models on large-scale synthetic datasets [Deitke et al. 2023] has also shown potential [Liu et al. 2024, 2023], although these methods are hindered by slow inference times.

An alternative strategy involves using multiplane image (MPI) representations, which approximate a scene using a series of parallel planes at fixed depths, each containing an image and alpha

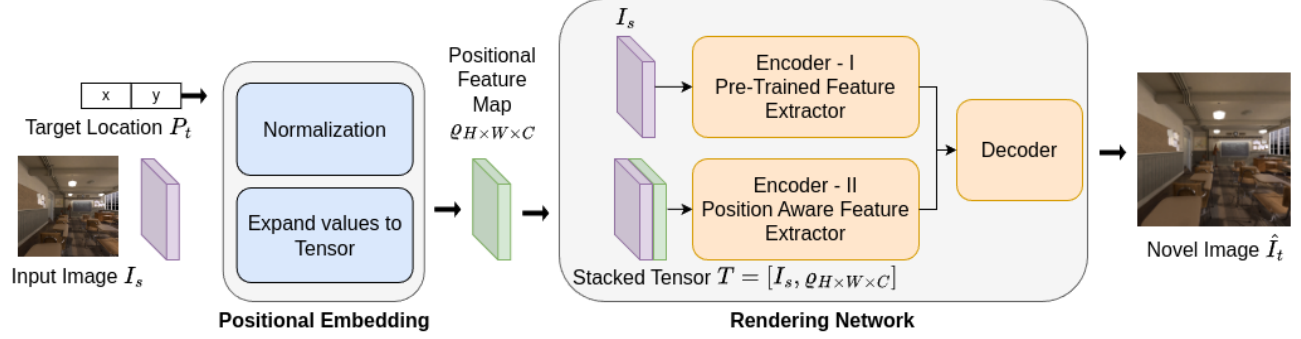


Fig. 1. Pipeline of Light Field Reconstruction using PLFNet which takes single input image I_s and target Sub-Aperture location $P_t = (x, y)$, and produces the image I_t .

map. This representation allows novel view generation based on a fixed [Flynn et al. 2019; Li and Kalantari 2020; Tucker and Snavely 2020; Zhou et al. 2018] or variable [Li and Kalantari 2020] number of planes. While MPI-based methods achieve superior visual quality, their computational demands remain high, especially during MPI layer prediction. Large-scale GANs [Koh et al. 2023] have also been explored for their ability to render fast and handle large baselines, though they introduce significant memory overhead, limiting their practicality.

More recent innovations, such as NViST [Jang and Agapito 2024], incorporate vision transformers (ViTs) [Dosovitskiy 2020] into view synthesis architectures, demonstrating strong generalization capabilities in real-world settings. By leveraging masked autoencoders (MAEs) and adaptive layer normalization conditioned on camera parameters, NViST delivers high-quality results, even for out-of-distribution scenes.

Our proposed method, PLFNet+ (described in Sec 4), contributes to the learning-based category by extending the views from a single input image while diverging from diffusion and transformer-based methods. By utilizing a lightweight design, PLFNet+ reduces computational overhead, enabling real-time rendering. This efficiency makes it particularly suited for dynamic environments where fast processing is crucial, addressing key challenges in the field of view synthesis.

3 Method: Light Field Reconstruction - PLFNet

We first define a Position Aware Light Field Reconstruction network called "PLFNet" which aims to reconstruct the LF from a single input image by iterative reconstructing individual sub-aperture images. The source image I_s serves as the basis for reconstructing the surrounding LF I_x , where \mathbf{x} represents the angular coordinate (x, y) , and s signifies the center of the $N \times N$ LF. Each sub-aperture image at location P_t , specified as $t \in \{(x_1, y_1), \dots, (x_N, y_N)\}$, undergoes reconstruction via:

$$\hat{I}_t = R(I_s, P_t), \quad (1)$$

This two stage pipeline has been shown in Figure 1

3.1 Positional Embedding

We define the target position by the coordinate vector $P_t = (x, y)$, where x , and y represent translations associated with angular coordinates. Given limited baseline shifts of LF reconstruction, directly using normalized values of P_t can suffice for training the network on discrete locations but querying for any continuous values of P_t .

Coordinate Normalization: The target coordinates $P_t(x, y)$ are normalized into $\bar{P}_t(\bar{x}, \bar{y})$ to ensure consistency across varying ranges of x, y . The normalization process is given by

$$\bar{P}_t = \left(\frac{x - x_{min}}{x_{max} - x_{min}}, \frac{y - y_{min}}{y_{max} - y_{min}} \right). \quad (2)$$

This normalization step ensures that the coordinates lie within a fixed range, which is crucial for subsequent encoding.

Input Channel: To incorporate the normalized coordinates into the network, the values of $\bar{P}_t = (\bar{x}, \bar{y})$ are expanded into a tensor $Q_{H \times W \times C}$, where the first channel holds the \bar{x} values, and the second channel holds the \bar{y} values

$$Q_{H \times W \times C} = [\bar{P}_t(\bar{x}), \bar{P}_t(\bar{y})], \quad C = 2. \quad (3)$$

This tensor has the same spatial resolution $H \times W$ as the input image, ensuring that positional information is aligned with the image features spatially.

3.2 Rendering Network

The role of the rendering network in PLFNet is to synthesize a novel target image I_t from the input image I_s and the positional embedding $Q_{H \times W \times C}$, obtained from the positional embedding stage. Our network architecture is inspired by LFSphereNet [Gond et al. 2023] and consists of two distinct encoder branches followed by a decoder network. These branches work in tandem to extract and merge spatial and positional features, ultimately generating high quality novel views.

The rendering network operates as follows: the first encoder processes the input image I_s to extract image-based features, while the second encoder processes both the input image I_s and the positional feature map $Q_{H \times W \times C}$ to capture position-dependent information. These features are subsequently merged in the decoder, which refines and upsamples the combined feature maps to generate the final output \hat{I}_t , a novel view at the target position.

3.2.1 Encoder I - Pre-trained Image Feature Extractor. The first encoder, E_1 , is a pre-trained image feature extractor that processes the input image I_s . Following the approach used in ResNet-152 [He et al. 2016], we utilize the initial layers of ResNet to extract lower-level feature maps that are rich in texture and local detail. Specifically, E_1 extracts a set of feature maps $F_1 \in \mathbb{R}^{h_1 \times w_1 \times 256}$, where h_1 and w_1 represent the spatial dimensions of the downsampled feature maps. These feature maps are then expanded to $F'_1 \in \mathbb{R}^{h_1 \times w_1 \times 512}$ through additional convolution layers to increase the depth of the feature space which can be described as

$$F'_1 = \text{Conv}(E_1(I_s)) \in \mathbb{R}^{h_1 \times w_1 \times 512}. \quad (4)$$

The extracted features F'_1 capture essential image content but lack positional awareness, which is handled by the second encoder.

3.2.2 Encoder II - Position-Aware Feature Extractor. The second encoder, E_2 , integrates both the input image I_s and the positional embedding $\varrho_{H \times W \times C}$ to adaptively capture position-specific features. Unlike the first encoder, which only processes the image, E_2 focuses on refining the feature maps based on the target position.

We first concatenate the input image I_s and the positional embedding $\varrho_{H \times W \times C}$ along the channel dimension, resulting in a stacked input tensor

$$T = [I_s, \varrho_{H \times W}] \in \mathbb{R}^{H \times W \times (3+C)}, \quad (5)$$

where C is the number of channels in ϱ . In our case, $C = 2$ for LF Reconstruction.

This stacked tensor T is passed through a series of convolutional layers that preserve the spatial dimensions, ensuring pixel-level positional information is retained throughout the encoding process, as demonstrated by LFSphereNet [Gond et al. 2023]. The encoder produces a feature map $F_2 \in \mathbb{R}^{H \times W \times d_3}$, where d_3 is the number of feature channels, and skip connections are generated from intermediate layers for later use in the decoder.

Formally, this can be expressed as

$$F_2 = E_2([I_s, \varrho_{H \times W}]) \in \mathbb{R}^{H \times W \times d_3}. \quad (6)$$

The skip connections, denoted as S_k , are collected from intermediate layers, where k indexes the corresponding layer, and are used to enhance spatial detail during the decoding stage.

3.2.3 View Decoder. The decoder, D , is responsible for merging the feature maps from both encoder branches and reconstructing the target image I_t at the desired target position. The concatenated feature maps F'_1 and F_2 are first combined along the channel dimension

$$F_{concat} = [F'_1, F_2] \in \mathbb{R}^{H \times W \times (512+d_3)}. \quad (7)$$

This concatenated feature map is then passed through a series of transposed convolution layers to progressively upsample the spatial resolution, ultimately matching the resolution of the input image. The decoder uses a combination of transposed convolutions and bilinear upsampling, preserving spatial coherence in the generated image. Skip connections S_k from the second encoder are concatenated into the upsampled feature maps at various stages to retain high-frequency details. The skip connections ensure that fine-grained positional and image details are retained, resulting in

more consistent and accurate novel views. The overall process can be expressed as

$$\hat{I}_t = D(F_{concat}, S_1, S_2, \dots, S_n) \in \mathbb{R}^{H \times W \times 3}. \quad (8)$$

The final output of the decoder is the synthesized target image \hat{I}_t , with spatial dimensions $H \times W$.

3.3 Training Loss

To optimize our PLFNet, we employ a combination of the L1 loss and the Multi-Scale Structural Similarity (MS-SSIM) [Wang et al. 2003] loss. This combination leverages the complementary strengths of each loss function. The L1 loss minimizes pixel-wise differences between the predicted sub-aperture images \hat{I}_t and the ground truth images I_t , which helps to maintain accurate reconstruction of intensity values. The MS-SSIM loss, on the other hand, is a perceptually motivated metric that focuses on preserving structural information and texture across multiple scales, which correlates better with human visual perception as shown in image restoration task [Zhao et al. 2016].

The total loss function L_{total} is defined as a weighted sum of the L1 and MS-SSIM losses

$$L_{total} = \alpha \cdot L_{L1} + (1 - \alpha) \cdot L_{MS-SSIM}, \quad (9)$$

where $\alpha = 0.80$ is a weighting factor that balances the contribution of the two losses. This combined loss function enables the network to generate high-quality light field reconstructions that are both pixel-accurate and perceptually consistent.

3.4 Implementation: PLFNet

The input of PLFNet is a single RGB image I_s and the target position $\varrho_{H \times W \times C}$. Here $H = 352$ and $W = 512$ which are similar to the spatial resolution of input image I_s . We set $C = 2$ because the datasets [Raj et al. 2016; Rerabek and Ebrahimi 2016; Srinivasan et al. 2017] are organized as a 2D grid, with only two angular coordinates considered. PLFNet was implemented in PyTorch and trained with the following hyperparameters: batch size of 24, learning rate of 0.003, adam optimizer, MS-SSIM and L1 loss. After each 30 epochs, the learning rate was decreased by a factor of 0.2. The network was trained for 150 epochs on 2 GPUs (Nvidia A40) within a computing cluster with Intel Xeon Gold 6338 CPUs. The training duration was 48 hrs. For the dataset split, 75% of the data was used for training, 12.5% for validation and 12.5% for testing.

4 Method: View Synthesis - PLFNet+

Our approach for view synthesis builds upon PLFNet by extending the positional embedding to handle wider baselines with translation along the z -axis. Here, I_t represents the synthesized image corresponding to the target viewpoint. Our approach consists of two key stages as shown in Figure 2: first, the target position is embedded into a high-dimensional space through positional embedding (discussed in Section 4.1), and second, novel views are rendered from these positions, which is detailed in Section 4.2.

4.1 Extended Positional Embedding

We define the target position by the coordinate vector $P_t = (x, y, z)$, where x , y , and z represent translations from the input image I_s . As

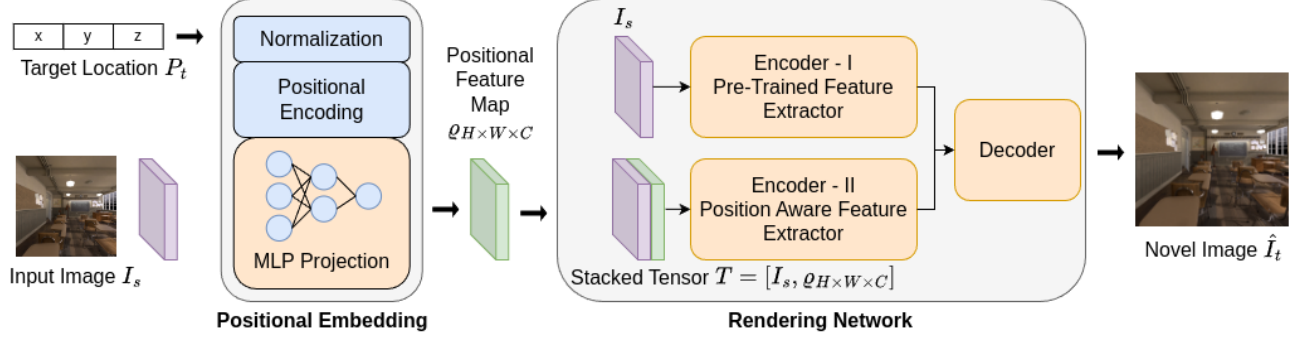


Fig. 2. Pipeline of view synthesis at larger baseline using PLFNet+ which takes single input image I_s & target location $P_t = (x, y, z)$, and produces the image I_t . The Positional embedding branch takes P_t and creates a higher dimensional projection of positional feature $\varrho_{H \times W \times C}$, which then along with input image I_s is passed to rendering network responsible for producing output image I_t .

the baseline increases and the search space extends along the z axis, it becomes necessary to project the target coordinates into a higher-dimensional space to accurately capture positional information. To address this, we employ a positional embedding strategy that combines positional encoding, inspired by NeRF [Mildenhall et al. 2021], along with a MLP for enhanced representation of the target coordinate P_t .

Coordinate Normalization: Similar to the normalization strategy in Section 3.1, we convert the target coordinates $P_t(x, y, z)$ into their normalized form $\bar{P}_t(\bar{x}, \bar{y}, \bar{z})$.

Positional Encoding: To project the normalized coordinates \bar{P}_t into a higher-dimensional space, we apply positional encoding. This involves concatenating multiple sine and cosine functions of varying frequencies

$$\gamma(\bar{P}_t) = \left(\dots, \cos\left(2\pi\sigma^{\frac{j}{m}}\bar{P}_t\right), \sin\left(2\pi\sigma^{\frac{j}{m}}\bar{P}_t\right), \dots \right), \quad (10)$$

where $\bar{P}_t = (\bar{x}, \bar{y}, \bar{z})$ is the normalized 3D coordinate vector, m represents the encoding depth, and $j \in \{0, \dots, m-1\}$. The parameter σ is a scaling constant based on the domain of \bar{P}_t . For our experiments, we use $m = 32$, therefore $2 \cdot m \cdot 3 = d_1$ yields an output of size $d_1 = 192$ dimensions, which provides enhanced positional awareness (see Table 6 for ablation study results).

Learning Based Projection: Once the positional encoding $\gamma(\bar{P}_t)$ has been computed, we further enhance the representation by passing it through an MLP. This MLP maps the low-dimensional encoded vector into a higher-dimensional space, and it has proven to work well with scene regression task as shown in NeRF [Mildenhall et al. 2021]. This process allows for a more expressive and flexible feature space, and our approach is similar to the adaptive layer normalization techniques used in NViST [Jang and Agapito 2024].

Let $\gamma(\bar{P}_t) \in \mathbb{R}^{1 \times d_1}$ be the output of the positional encoding, where d_1 is the dimensionality of the encoding. The MLP projects this vector into a high-dimensional space $\mathbb{R}^{1 \times d_2}$, where d_2 is chosen based on the desired resolution. Mathematically, the projection is represented as

$$\rho = \text{MLP}(\gamma(\bar{P}_t)) \in \mathbb{R}^{1 \times d_2}. \quad (11)$$

After this, the vector ρ is reshaped into a feature map of size $h \times w$, where $d_2 = hw$. This reshaping operation can be expressed

using the inverse vectorization notation as

$$\varrho_{h \times w} = \text{vec}^{-1}(\rho) \in \mathbb{R}^{h \times w}. \quad (12)$$

Finally, the feature map $\varrho_{h \times w}$ is upsampled to match the spatial resolution of the input image, denoted by $H \times W$. This upsampling is performed using a scaling factor $\alpha = \frac{H}{h} = \frac{W}{w}$, as follows

$$\varrho_{H \times W} = \text{Upsample}(\varrho_{h \times w}, \alpha) \in \mathbb{R}^{H \times W}. \quad (13)$$

The final upsampled representation $\varrho_{H \times W}$ retains the positional information of the target coordinate and is subsequently used by the rendering network to generate the novel view.

4.2 Rendering Network

The rendering network remains similar to Section 3.2. However, in the case of view synthesis, the positional embedding is denoted by a single channel, simplifying the input to the second encoder as

$$T = [I_s, \varrho_{H \times W}] \in \mathbb{R}^{H \times W \times (3+1)}. \quad (14)$$

The output of the rendering network is the target image \hat{I}_t .

4.3 Training Loss

For the view synthesis task, we extend the loss function previously defined in Section 3.3 to better capture fine-grained details, especially with larger baselines. We maintain the same combination of L1 loss and MS-SSIM loss, which focuses on minimizing pixel-wise differences and preserving structural consistency, respectively. However, to further enhance the quality of the synthesized views, particularly in the frequency domain, we incorporate the Focal Frequency Loss (FFL) [Jiang et al. 2021] into the total loss function.

The FFL addresses the spectral bias in neural networks by adaptively focusing on the frequency components that are hardest to synthesize. This allows the model to improve the reconstruction of high-frequency details, which are critical for realistic novel view generation.

The FFL is defined as

$$L_{\text{FFL}} = \frac{1}{MN} \sum_{u=0}^{M-1} \sum_{v=0}^{N-1} w(u, v) |F_r(u, v) - F_f(u, v)|^2, \quad (15)$$

where $F_r(u, v)$ and $F_f(u, v)$ represent the real and predicted frequency components at position (u, v) in the Fourier domain, and

$w(u, v)$ is a dynamic spectrum weight that emphasizes hard-to-synthesize frequencies.

Thus, the total loss function $L_{\text{total}+}$ for PLFNet+ is updated to

$$L_{\text{total}+} = \alpha \cdot L_{\text{L1}} + (1 - \alpha) \cdot L_{\text{MS-SSIM}} + \beta \cdot L_{\text{FFL}}, \quad (16)$$

where L_{FFL} is the Focal Frequency Loss, and β is a weight balancing its contribution relative to the L1 and MS-SSIM losses.

This augmented loss function allows PLFNet+ to generate sharper, more realistic novel views by not only optimizing for spatial accuracy but also addressing frequency domain discrepancies.

4.4 Implementation: PLFNet+

We keep the same implementation as in PLFNet (described in Section 3.4, but set $H = 512$, $W = 512$). We also set $C = 1$ as the positional maps is single channel. Due to limitation of training data when using our synthetic dataset we employ multi stage training strategies to reach satisfactory results in training process.

4.4.1 Multi Stage Training. Given the scarcity of large-scale datasets for view synthesis with wide baselines, we adopt a three-stage training approach shown in Figure 3 to progressively enhance the network’s ability to capture image features and handle positional shifts.

Stage 1 serves as a preconditioning step, training the network on a large-scale light field dataset [Srinivasan et al. 2017]. While the baseline between the views in each light field is relatively narrow, the dataset’s large scale enables the network to learn both high- and low-level image features, implicitly understanding depth. In this stage, the network is conditioned to synthesize novel views within a constrained light field volume, similar to the reconstruction process described in PLFNet (Section 3). Once the network demonstrates proficiency in this task, we transition to the next stage.

Stage 2 introduces a dataset with a significantly larger baseline: the Spherical Light Field Database (SLFDB) [Zerman et al. 2024], which consists of 20 spherical light fields captured with 60 angular dimensions. From these omnidirectional images (ODIs), we extract planar patches and fine-tune the network with a lower learning rate. This step enables the network to learn to handle wider baseline movements while maintaining positional accuracy. Following this, the network is prepared for the final stage of training, which focuses on the joint optimization of the MLP and rendering network with more random positions.

Stage 3 involves training the network on a synthetic dataset containing random camera viewpoints within an $N \times N \times N$ cubical volume. The increase in the spatial search space necessitates the use of the positional embedding module for accurate view synthesis. In this stage, the network is fine-tuned to handle more complex camera translations and larger scene variations, fully utilizing the positional embedding to enhance rendering precision.

5 Experimental Evaluation

In this section, we present a comprehensive evaluation of our proposed PLFNet and PLFNet+ architectures. We begin by assessing the performance of PLFNet+ for view synthesis on datasets with varying baselines and complexities. Following this, we demonstrate the capability of PLFNet in reconstructing full light fields from a

single input image. The experiments for view synthesis are detailed in Section 5.1, while light field reconstruction results are discussed in Section 5.2.

5.1 View Synthesis

5.1.1 Datasets. To evaluate the performance of PLFNet+ on view synthesis, we used two datasets. The first is a custom Blender dataset, created specifically for this task, which contains images from different scenes with camera movements constrained within a 20 cm cubical volume. The second dataset is COCO [Caesar et al. 2018], which we use during training in the same manner as AdaMPI [Han et al. 2022], where depth-image-based rendering (DIBR) with hole filling is employed to generate the training data. During evaluation, we take an input image and synthesize a novel image at a specified target location. The synthesized image is then treated as input to generate an image back at the original location. This process enables us to compare the reconstructed image with the ground truth, which is the original input image, allowing for an assessment of rendering quality. Both datasets are evaluated at resolutions of 256×256 and 512×512 and a movement within a volume of 20 cm^3 .

5.1.2 Evaluation Metrics. To objectively evaluate the quality of the synthesized novel views, we employed multiple standard and advanced metrics. These include peak signal-to-noise ratio (PSNR) and structural similarity index measure (SSIM) [Wang et al. 2004], as well as multi-scale structural similarity index measure (MS-SSIM) [Wang et al. 2003], pixel- based visual information fidelity (VIFP) [Sheikh and Bovik 2006], deep image structure and texture similarity (DISTS) [Ding et al. 2020], and learned perceptual image patch similarity (LPIPS) [Zhang et al. 2018]. These metrics capture not only pixel-level errors but also perceptual differences, providing a holistic view of the synthesis quality.

5.1.3 Results. Quantitative Results: The quantitative results for view synthesis across different datasets and resolutions are presented in Table 1. Our proposed PLFNet+ consistently outperforms AdaMPI [Han et al. 2022] on the Blender dataset and achieves competitive results on the COCO [Caesar et al. 2018] dataset. Although AdaMPI demonstrates slightly better performance in perceptual metrics such as DISTS and LPIPS, our method remains competitive across a range of metrics, especially on PSNR and SSIM.

Interestingly, we observe a slight performance drop in AdaMPI and PLFNet+ when increasing the resolution from 256×256 to 512×512 . This highlights the challenges of scaling models without increasing their capacity to handle higher-resolution inputs. In contrast to other methods that explicitly rely on depth estimation using the DPT model, our approach learns scene depth implicitly from RGB input alone, demonstrating the flexibility of our method without the need for pre-computed depth maps.

When evaluating inference time, PLFNet+ excels, particularly at higher resolutions. As shown in Table 2, our method achieves an inference time of 0.0086 seconds for a resolution of 512×512 , outperforming all other methods by a significant margin. This makes PLFNet+ highly suitable for real-time applications, where rapid generation of novel views is critical, such as in dynamic video streams or interactive virtual environments.

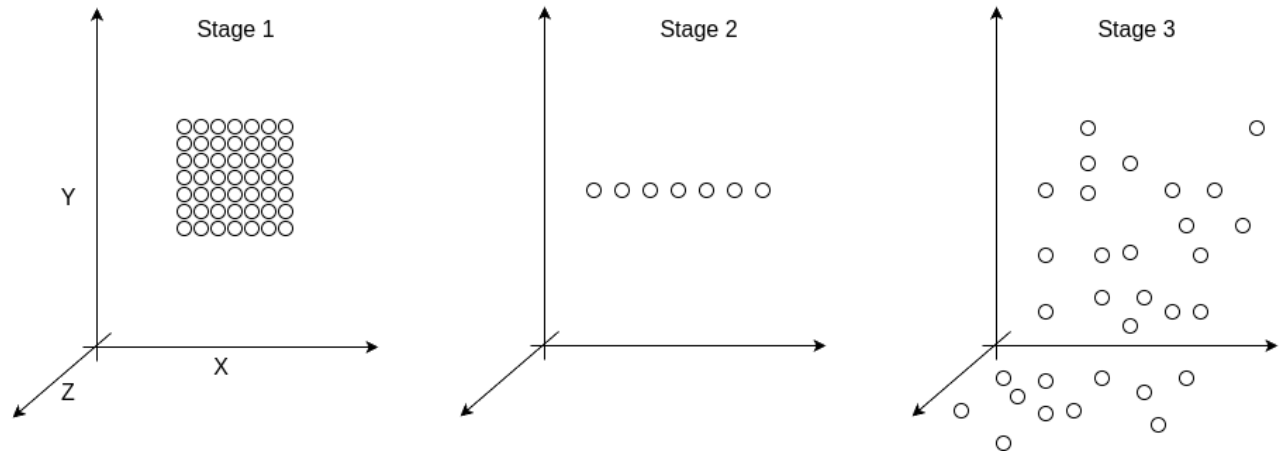


Fig. 3. Conceptual view of camera placement of each stage of training. Stage 1 involves small baseline and a fixed grid of camera, stage 2 focuses on larger baseline but still keep the discrete placement of cameras on a fixed grid. Finally, stage 3 trains the network on large baseline with random camera placements in a cubical volume.

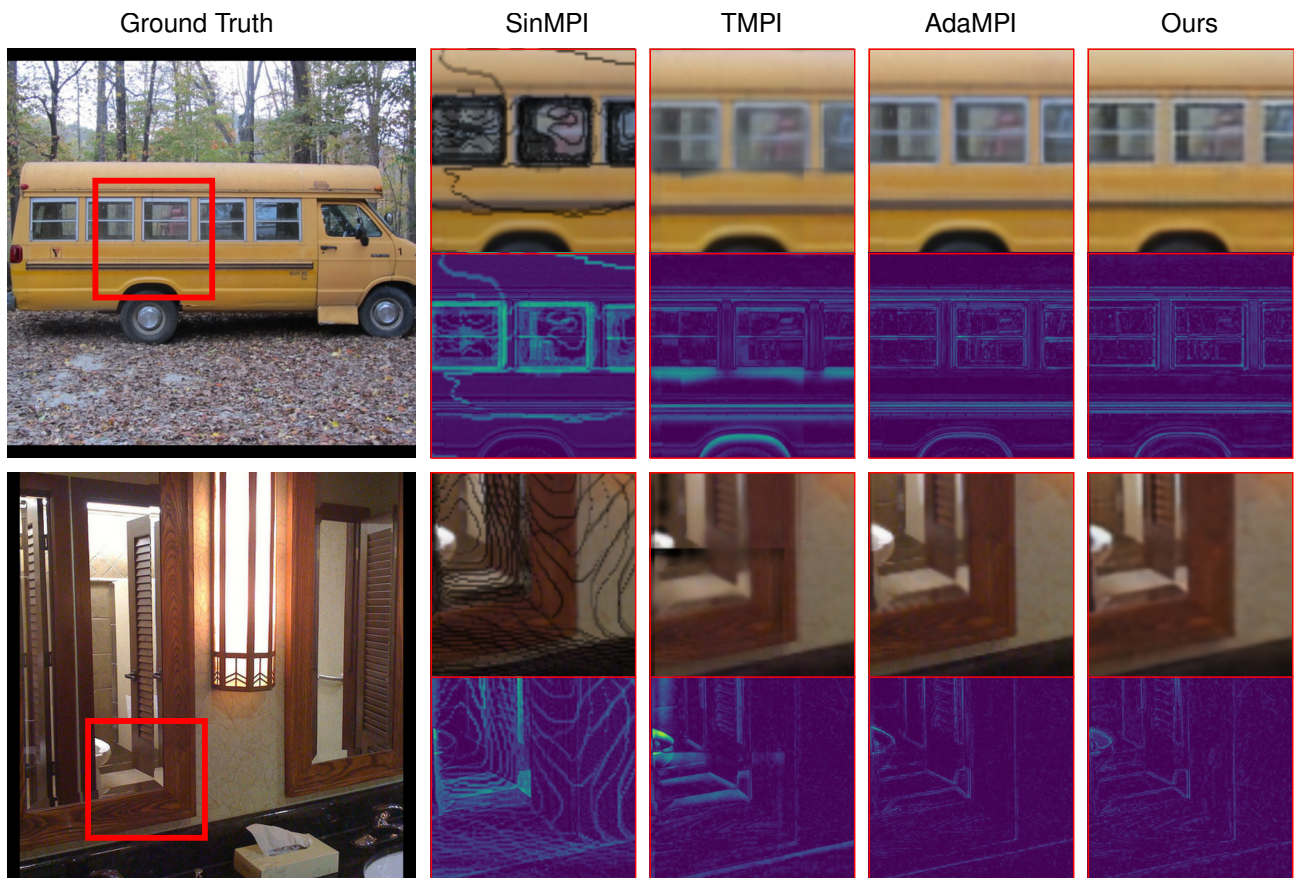


Fig. 4. Comparison of view synthesis results on COCO dataset with error maps for SinMPI [Pu et al. 2023], TMPI [Khan et al. 2023], AdaMPI [Han et al. 2022], and our method. The top and bottom rows depict the synthesized views for two different scenes, with corresponding error maps underneath. The red rectangles highlight specific regions of interest to emphasize differences in synthesis accuracy and visual fidelity.

Table 1. View Synthesis Results (best values in bold): Quantitative comparison of view synthesis methods on Blender (256x256 and 512x512) and COCO (256x256 and 512x512) datasets. PLFNet+ (Ours) achieves the best overall results on the Blender dataset across most metrics, significantly outperforming previous methods. On the COCO dataset, PLFNet+ demonstrates strong performance, achieving the second-best scores, particularly excelling in SSIM and MS-SSIM, closely trailing AdaMPI. These results highlight PLFNet+’s capability to generate high-quality novel views with competitive accuracy, especially in complex real-world settings like COCO.

Dataset	Method	PSNR \uparrow	SSIM \uparrow	MS-SSIM \uparrow	VIFP \uparrow	DISTS \downarrow	LPIPS \downarrow
Blender 256x256	SinMPI [Pu et al. 2023]	17.3295	0.4193	0.7064	0.4911	0.2794	0.4097
	TMPI [Khan et al. 2023]	19.9507	0.7160	0.8264	0.4822	0.1458	0.1471
	AdaMPI [Han et al. 2022]	24.9252	0.8092	0.9145	0.6720	0.0680	0.0455
	PLFNet+ (Ours)	28.8023	0.9003	0.9655	0.7516	0.1586	0.1007
Blender 512x512	SinMPI [Pu et al. 2023]	18.3441	0.4599	0.6885	0.3621	0.2251	0.3966
	TMPI [Khan et al. 2023]	20.0126	0.7071	0.8070	0.3605	0.1268	0.1640
	AdaMPI [Han et al. 2022]	23.1416	0.7510	0.8566	0.4353	0.0751	0.0770
	PLFNet+ (Ours)	26.3339	0.8334	0.9307	0.5633	0.2191	0.1947
COCO [Caesar et al. 2018] 256x256	SinMPI [Pu et al. 2023]	14.5548	0.4271	0.6621	0.3706	0.2867	0.4024
	TMPI [Khan et al. 2023]	17.1759	0.5454	0.7314	0.3819	0.2028	0.2415
	AdaMPI [Han et al. 2022]	23.6155	0.8263	0.9345	0.7232	0.1055	0.0797
	PLFNet+ (Ours)	22.8933	0.7608	0.9070	0.5534	0.2378	0.2560
COCO [Caesar et al. 2018] 512x512	SinMPI [Pu et al. 2023]	15.7272	0.4740	0.6712	0.3095	0.2392	0.3775
	TMPI [Khan et al. 2023]	18.1375	0.5444	0.7499	0.2906	0.1750	0.2758
	AdaMPI [Han et al. 2022]	21.5931	0.7425	0.8925	0.5215	0.1156	0.1559
	PLFNet+ (Ours)	20.2596	0.6229	0.8001	0.3007	0.2758	0.4226

Table 2. Inference time (in seconds) to render the novel view for different resolutions on RTX 2070 Super or and frames per second (in seconds / fps). Best values in bold. The fps values are rounded down for simplicity.

Method	256x256	512x512
SinMPI [Pu et al. 2023]	0.0752 / 13	0.2368 / 4
TMPI [Khan et al. 2023]	0.0910 / 11	0.2640 / 4
AdaMPI [Han et al. 2022]	0.2261 / 4	0.3254 / 3
PLFNet+ (Ours)	0.0074 / 135	0.0086 / 116

Qualitative Results: Figure 4 provides a visual comparison of the view synthesis results for different methods on the COCO dataset. Each method’s output is accompanied by error maps, allowing for a more detailed analysis of their accuracy.

SinMPI [Pu et al. 2023] struggles with rendering artifacts, particularly in regions with complex textures and geometry, as evidenced by the error maps. These issues are likely a result of its depth estimation and scene representation. TMPI [Khan et al. 2023] also displays notable tiling artifacts due to its approach of partitioning the scene into multiple planes, leading to visible seams and discontinuities.

In contrast, both AdaMPI and our proposed PLFNet+ produce the most visually accurate results, with minimal artifacts. AdaMPI shows slightly better performance in some scenarios, particularly in handling fine details, but our method’s ability to efficiently handle reflections, occlusions, and fine textures stands out. While AdaMPI may have a slight edge in perceptual quality, our method’s superior inference speed makes it the more practical choice for real-time applications, balancing high-quality synthesis with the demands of time-sensitive environments.

5.2 Extending View Synthesis: Light Field Reconstruction

5.2.1 Datasets. For LF reconstruction, we evaluated our method using three publicly available datasets: Lytro Flowers [Srinivasan et al. 2017], Stanford Light Field Archive [Raj et al. 2016], and JPEG-Pleno [Rerabek and Ebrahimi 2016]. These datasets are widely used for benchmarking light field reconstruction algorithms. The extracted light field images had dimensions of 352x512 with a 7x7 angular resolution.

We trained PLFNet on 75% of the Lytro Flowers and Stanford datasets, with the remaining 25% reserved for testing. The JPEG-Pleno dataset, however, was exclusively used for testing to evaluate the generalization capability of our model, as it was not included in the training process.

5.2.2 Evaluation Metrics. We utilize similar evaluation metrics as described in Section 5.1.2. Since the light field reconstruction works in very narrow baseline between each sub-aperture image, and has discrete camera locations, the search space is much smaller therefore we get much better scores in these metrics.

5.2.3 Results. Quantitative Results: The quantitative results of our light field reconstruction experiments are presented in Table 3.

Table 3. LF Reconstruction: Quality, best values in bold, second best in *italics*. Arrows indicate the better direction

Dataset	Method	PSNR \uparrow	SSIM \uparrow	MS-SSIM \uparrow	VIFP \uparrow	DISTS \downarrow	LPIPS \downarrow
Flowers [Srinivasan et al. 2017]	NoisyLFRecon	<i>39.9500</i>	0.9763	0.9932	0.9285	0.0389	0.0190
	DGLF	35.6194	0.8773	0.9301	0.6021	0.1556	0.1431
	DALF	37.3006	0.8941	0.9589	0.7362	0.1033	0.0911
	IR-V	37.9034	0.9122	0.9645	0.7324	0.0994	0.0707
	LFSphereNet	41.3719	0.9461	0.9868	0.9060	0.0812	0.0512
	PLFNet	37.2606	<i>0.9601</i>	<i>0.9914</i>	<i>0.9062</i>	<i>0.0608</i>	<i>0.0229</i>
Stanford [Raj et al. 2016]	NoisyLFRecon	35.4917	0.9572	0.9771	0.8380	0.0718	0.0395
	DGLF	35.6509	0.9673	<i>0.9897</i>	0.8655	0.0685	0.0321
	DALF	38.2996	0.9172	0.9750	0.7829	0.0667	0.0402
	IR-V	<i>39.4909</i>	0.9440	0.9852	0.8358	0.0628	0.0390
	LFSphereNet	40.9830	0.9488	0.9797	0.8842	<i>0.0556</i>	<i>0.0300</i>
	PLFNet	36.8530	<i>0.9601</i>	0.9927	<i>0.8679</i>	0.0553	0.0182
JPEG Pleno [Rerabek and Ebrahimi 2016]	NoisyLFRecon	36.6275	0.9575	0.9687	0.8549	<i>0.0718</i>	0.0435
	DGLF	32.3387	0.7207	0.8166	0.4246	0.1556	0.1431
	DALF	35.0285	0.8257	0.9291	0.6462	0.1095	0.0937
	IR-V	<i>37.2085</i>	0.9122	0.9719	0.7878	0.0894	0.0605
	LFSphereNet	39.2624	<i>0.9429</i>	0.9879	0.9069	0.0737	<i>0.0425</i>
	PLFNet	33.8982	0.9106	<i>0.9838</i>	<i>0.8683</i>	0.0590	0.0261

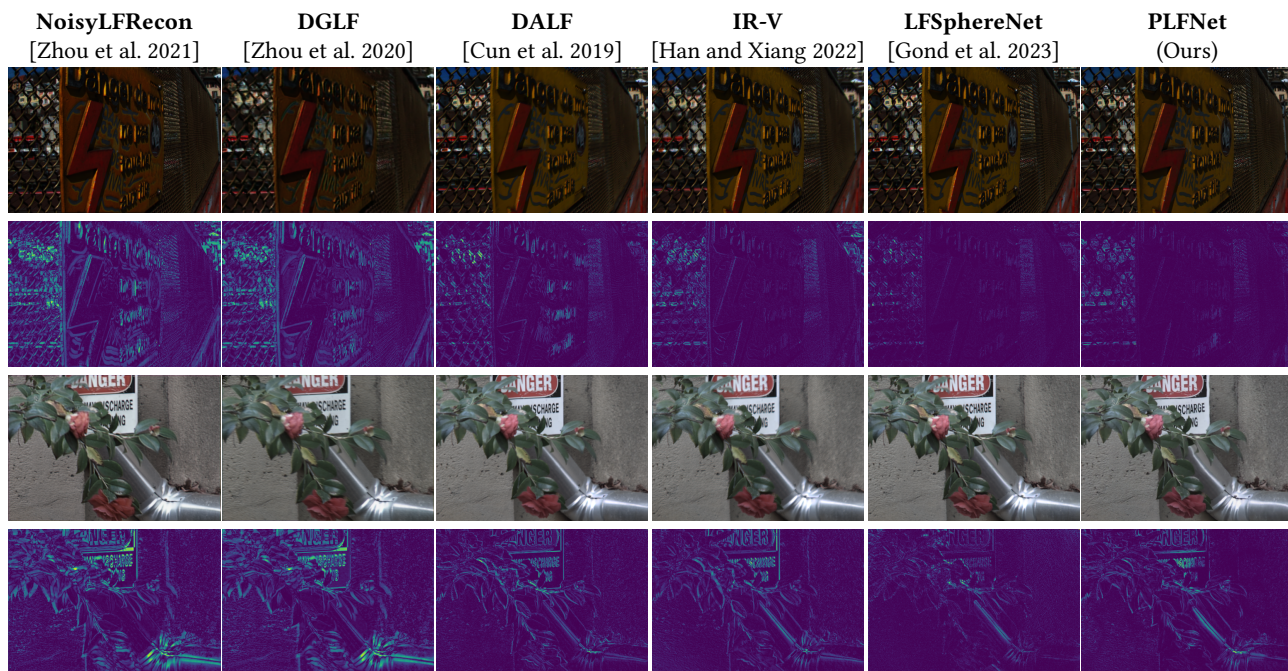


Fig. 5. Qualitative results for planar light field reconstruction. We compare results (from left to right) of NoisyLFRecon [Zhou et al. 2021], DGLF [Zhou et al. 2020], DALF [Cun et al. 2019], IR-V [Han and Xiang 2022], LFSphereNet [Gond et al. 2023] and PLFNet (Ours). We have rendered top right sub-aperture image of a $352 \times 512 \times 7 \times 7$ planar light field. First two rows shows an image with error map from JPEG Pleno dataset, and last two rows show an image with error map from Stanford dataset.

Our proposed PLFNet demonstrates competitive performance compared to state-of-the-art methods, including NoisyLFRecon [Zhou et al. 2021], DGLF [Zhou et al. 2020], DALF [Cun et al. 2019], IR-V [Han and Xiang 2022], and LFSphereNet [Gond et al. 2023]. All

models were trained from scratch using identical datasets for a fair comparison. Publicly available implementations were used for the methods by Zhou et al. [2020, 2021] and Han and Xiang [2022], while

Table 4. Inference time for LF reconstruction of size $352 \times 512 \times 7 \times 7$. The inference time has been logged on GTX 1080 Ti

Method	Purpose	Inference Time (s)
NoisyLFRecon	LF reconstruction	1.1830
DGLF	LF reconstruction	1.5009
DALF	LF reconstruction	0.0583
IR-V	LF reconstruction	0.1429
LFsphereNet	LF reconstruction	0.0008
PLFNet	Novel view synthesis	0.0980

DALF [Cun et al. 2019] was re-implemented in PyTorch according to the original paper.

Although DGLF and LFSphereNet generate the full $N \times N$ light field in a single pass, both DALF and our PLFNet reconstruct each sub-aperture image iteratively. For the Stanford dataset, which offers fewer training samples compared to Lytro Flowers, LFSphereNet delivered the best results across most metrics, with PLFNet showing competitive performance, particularly excelling in SSIM and MS-SSIM. In terms of computational efficiency, PLFNet demonstrated significant improvements as shown in Table 4. Our PLFNet achieved an inference time of **0.0980** seconds for whole LF reconstruction which included $7 \times 7 = 49$ forward passes. However, per view inference on average is around 0.006 seconds highlighting its potential for real-time applications.

Qualitative Results: The qualitative evaluation of light field reconstruction is illustrated in Figure 5. We compare the visual performance of our proposed PLFNet against state-of-the-art methods for light field views, focusing on the top right corner sub-aperture view. The first two rows depict reconstruction results for the JPEG-Pleno [Rerabek and Ebrahimi 2016] dataset. In these challenging scenarios, PLFNet demonstrates superior reconstruction quality with fewer visible artifacts, as evident in the error maps. Compared to LFSphereNet [Gond et al. 2023], which also shows strong performance, PLFNet exhibits more accurate details and reduced error magnitudes, highlighting its robustness and generalization capabilities. The subsequent rows display results for the Stanford Light Field Archive [Raj et al. 2016] dataset. Here, our method consistently outperforms NoisyLFRecon [Zhou et al. 2021], which utilizes nine input images for reconstruction. Despite this advantage, NoisyLFRecon produces noticeable artifacts and blurring in regions with fine structures. In contrast, PLFNet, which relies on only a single input image, achieves sharper reconstructions with more faithful reproduction of scene geometry and textures. This indicates that PLFNet can effectively capture and synthesize complex light field information even with minimal input data.

Overall, the qualitative results corroborate the quantitative findings, showcasing ability of PLFNet to achieve high-quality reconstructions with low error rates. This performance shows potential for practical applications where high-fidelity light field reconstruction from sparse data is required.

6 Ablation Study

In this section, we present a two-part ablation study to assess the effectiveness of our proposed method, focusing on positional understanding and the impact of different positional embedding techniques. The first part evaluates the performance of PLFNet+ under varying sparse input configurations, demonstrating how the number and location of input images influence view synthesis. The second part investigates the contribution of different positional encoding strategies to the overall reconstruction quality, highlighting the role of each component in our final model.

6.1 Sparse Input Mode

The first part of the ablation study explores how the performance of PLFNet+ is affected by varying the number and position of input images for view synthesis. We evaluate three configurations: (i) a single central image as input, (ii) a single image from a random location within the cubical volume, and (iii) two images from random locations. These setups allow us to understand how well the model generalizes to sparse input scenarios, particularly in cases where inputs are not centrally aligned.

Table 5 presents the quantitative results of this study. As expected, the single central view input yields the best performance across all metrics, with a PSNR of 28.8023 and SSIM of 0.9009, indicating that the model performs best when provided with a centrally located reference image. The random input configurations, whether with one or two images, exhibit slightly reduced performance, suggesting that while the model can generalize to inputs from random locations, the quality of the synthesized view degrades with less structured input data. Nevertheless, even with these random inputs, PLFNet+ achieves acceptable performance, demonstrating its robustness in handling diverse input scenarios.

6.2 Positional Embedding

In the second part of the ablation study, we analyze the impact of different positional embedding strategies on view synthesis. We compare four configurations: (i) MLP only, (ii) normalization only, (iii) normalization with positional encoding, (iv) normalization with MLP, and (v) the full setup with normalization, positional encoding, and MLP. This analysis aims to determine the contribution of each component in enhancing the model’s understanding of positional information.

The results are summarized in Table 6. The combination of normalization, positional encoding, and MLP consistently outperforms the other configurations, achieving a PSNR of 28.8023 and SSIM of 0.9003. This demonstrates the effectiveness of our final proposed method in capturing positional variations and synthesizing accurate novel views. By contrast, using only normalization or MLP leads to a noticeable drop in performance specially in high frequency regions, underscoring the importance of combining these techniques to achieve optimal results.

The setup with normalization and MLP alone performs better than using MLP in isolation but still falls short of the complete configuration. These findings highlight the critical role of positional

Table 5. View Synthesis Results with Sparse Input Mode: Quality, best values in bold

Number of Input Images	PSNR \uparrow	SSIM \uparrow	MS-SSIM \uparrow	VIFP \uparrow	DISTS \downarrow	LPIS \downarrow
2 Images - Random Location	23.0571	0.7444	0.8462	0.4297	0.2782	0.2510
1 Image - Random Location	22.8429	0.7243	0.8386	0.3524	0.3373	0.3703
1 Image - Central View	28.8023	0.9003	0.9655	0.7516	0.1586	0.1007

encoding and MLP in providing a richer representation of the 3D positional information, which is essential for accurately reconstructing complex novel views.

7 Conclusion

In this paper we presented a novel, lightweight, position-aware network for real-time view synthesis and light field reconstruction, which leverages a position-aware embedding combined with a rendering network to achieve both efficiency and high visual quality. Through the development of PLFNet and its extension, PLFNet+, our approach demonstrates superior synthesis quality, particularly in handling complex translational movements without relying on computationally intensive operations like warping.

Extensive evaluations reveal that PLFNet+ achieves a strong balance between visual fidelity and inference speed, positioning it as a feasible solution for applications requiring real-time performance, such as telepresence and augmented reality. Additionally, our network architecture shows robustness in various scenarios, from narrow to wide baseline settings, making it adaptable to dynamic and interactive environments.

The promising results from ablation studies underscore the effectiveness of our positional embedding design, particularly the integration of normalization, positional encoding, and MLP components. Overall, our work provides a significant step towards more accessible, high-performance view synthesis frameworks, paving the way for broader application in consumer and industrial devices.

Acknowledgments

The work was supported by the European Joint Doctoral Programme on Plenoptic Imaging (PLENOPTIMA) through the European Union’s Horizon 2020 research and innovation programme under the Marie Skłodowska-Curie Grant Agreement No. 956770. The computations were enabled by resources provided by the National Academic Infrastructure for Supercomputing in Sweden (NAISS), partially funded by the Swedish Research Council through grant agreement no. 2022-06725. We thank the High Performance Computing Center North (HPC2N) at Umeå University for providing computational resources and valuable support during test and performance runs.

References

Kyuhoo Bae, Andre Ivan, Hajime Nagahara, and In Kyu Park. 2021. 5d light field synthesis from a monocular video. In *2020 25th International Conference on Pattern Recognition (ICPR)*. IEEE, 7157–7164.

Jonathan T Barron, Ben Mildenhall, Matthew Tancik, Peter Hedman, Ricardo Martin-Brualla, and Pratul P Srinivasan. 2021. Mip-nerf: A multiscale representation for anti-aliasing neural radiance fields. In *Proceedings of the IEEE/CVF international conference on computer vision*. 5855–5864.

Holger Caesar, Jasper Uijlings, and Vittorio Ferrari. 2018. Coco-stuff: Thing and stuff classes in context. In *Proceedings of the IEEE conference on computer vision and pattern recognition*. 1209–1218.

Paramanand Chandramouli, Kanchana Vaishnavi Gandikota, Andreas Goerlitz, Andreas Kolb, and Michael Moeller. 2020. A generative model for generic light field reconstruction. *IEEE Transactions on Pattern Analysis and Machine Intelligence* 44, 4 (2020), 1712–1724.

Bin Chen, Lingyan Ruan, and Miu-Ling Lam. 2020. LFGAN: 4D Light Field Synthesis from a Single RGB Image. *ACM Trans. Multimedia Comput. Commun. Appl.* 16 (2 2020), Issue 1. <https://doi.org/10.1145/3366371>

Xiaodong Cun, Feng Xu, Chi-Man Pun, and Hao Gao. 2019. Depth-Assisted Full Resolution Network for Single Image-Based View Synthesis. *IEEE Computer Graphics and Applications* 39 (2019), 52–64. Issue 2. <https://doi.org/10.1109/MCG.2018.2884188>

Matt Deitke, Dustin Schwenk, Jordi Salvador, Luca Weihs, Oscar Michel, Eli VanderBilt, Ludwig Schmidt, Kiana Ehsani, Aniruddha Kembhavi, and Ali Farhadi. 2023. Objaverse: A universe of annotated 3d objects. In *Proceedings of the IEEE/CVF Conference on Computer Vision and Pattern Recognition*. 13142–13153.

Elijs Dima and Mårten Sjöström. 2021. Camera and Lidar-Based View Generation for Augmented Remote Operation in Mining Applications. *IEEE Access* 9 (2021), 82199–82212.

Keyan Ding, Kede Ma, Shiqi Wang, and Eero P Simoncelli. 2020. Image quality assessment: Unifying structure and texture similarity. *IEEE transactions on pattern analysis and machine intelligence* 44, 5 (2020), 2567–2581.

Alexey Dosovitskiy. 2020. An image is worth 16x16 words: Transformers for image recognition at scale. *arXiv preprint arXiv:2010.11929* (2020).

John Flynn, Michael Broxton, Paul Debevec, Matthew DuVall, Graham Fyffe, Ryan Overbeck, Noah Snavely, and Richard Tucker. 2019. DeepView: View Synthesis With Learned Gradient Descent. In *Proceedings of the IEEE/CVF Conference on Computer Vision and Pattern Recognition (CVPR)*.

Sara Fridovich-Keil, Alex Yu, Matthew Tancik, Qinlong Chen, Benjamin Recht, and Angjoo Kanazawa. 2022. Plenoxels: Radiance fields without neural networks. In *Proceedings of the IEEE/CVF conference on computer vision and pattern recognition*. 5501–5510.

Manu Gond, Emin Zeman, Sebastian Knorr, and Mårten Sjöström. 2023. LFSphereNet: Real Time Spherical Light Field Reconstruction from a Single Omnidirectional Image. In *Proceedings of the 20th ACM SIGGRAPH European Conference on Visual Media Production*. 1–10.

Kang Han and Wei Xiang. 2022. Inference-Reconstruction Variational Autoencoder for Light Field Image Reconstruction. *IEEE Transactions on Image Processing* 31 (2022), 5629–5644. <https://doi.org/10.1109/TIP.2022.3197976>

Yuxuan Han, Ruicheng Wang, and Jialong Yang. 2022. Single-view view synthesis in the wild with learned adaptive multiplane images. In *ACM SIGGRAPH 2022 Conference Proceedings*. 1–8.

Kaiming He, Xiangyu Zhang, Shaoqing Ren, and Jian Sun. 2016. Deep residual learning for image recognition. In *Proceedings of the IEEE conference on computer vision and pattern recognition*. 770–778.

Aaron Isaksen, Leonard McMillan, and Steven J Gortler. 2000. Dynamically reparameterized light fields. In *Proceedings of the 27th annual conference on Computer graphics and interactive techniques*. 297–306.

Andre Ivan, In Kyu Park, et al. 2019. Synthesizing a 4D spatio-angular consistent light field from a single image. *arXiv preprint arXiv:1903.12364* (2019).

Wonbong Jang and Lourdes Agapito. 2024. NViST: In the Wild New View Synthesis from a Single Image with Transformers. In *Proceedings of the IEEE/CVF Conference on Computer Vision and Pattern Recognition*. 10181–10193.

Liming Jiang, Bo Dai, Wayne Wu, and Chen Change Loy. 2021. Focal frequency loss for image reconstruction and synthesis. In *Proceedings of the IEEE/CVF international conference on computer vision*. 13919–13929.

Bernhard Kerbl, Georgios Kopanas, Thomas Leimkühler, and George Drettakis. 2023. 3D Gaussian Splatting for Real-Time Radiance Field Rendering. *ACM Trans. Graph.* 42, 4 (2023), 139–1.

Numair Khan, Lei Xiao, and Douglas Lanman. 2023. Tiled multiplane images for practical 3d photography. In *Proceedings of the IEEE/CVF International Conference on Computer Vision*. 10454–10464.

Jing Yu Koh, Harsh Agrawal, Dhruv Batra, Richard Tucker, Austin Waters, Honglak Lee, Yinfei Yang, Jason Baldrige, and Peter Anderson. 2023. Simple and effective synthesis of indoor 3d scenes. In *Proceedings of the AAAI Conference on Artificial Intelligence*, Vol. 37. 1169–1178.

Marc Levoy and Pat Hanrahan. 1996. Light field rendering. In *Proceedings of the 23rd annual conference on Computer graphics and interactive techniques*. 31–42.

Table 6. View Synthesis Results with Different Positional Embedding Methods: Quality, best values in bold

Positional Embedding	PSNR \uparrow	SSIM \uparrow	MS-SSIM \uparrow	VIFP \uparrow	DISTS \downarrow	LPIPS \downarrow
MLP	23.2578	0.7633	0.8686	0.4063	0.2566	0.2726
Normalization	25.2855	0.8376	0.9256	0.5309	0.2132	0.1680
Norm+Positional Encoding	24.1945	0.7941	0.8962	0.4502	0.2276	0.1946
Norm+MLP	26.4475	0.8508	0.9421	0.6247	0.2119	0.1647
Norm+PosEnc+MLP	28.8023	0.9003	0.9655	0.7516	0.1586	0.1007

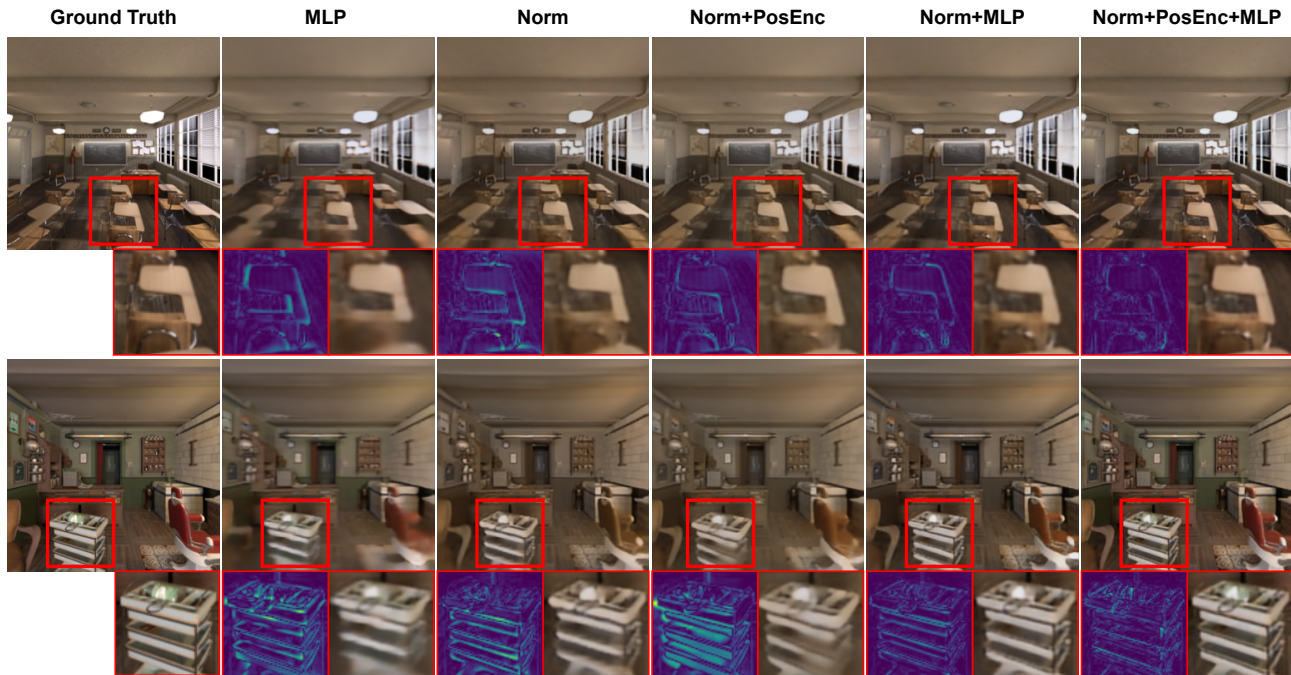


Fig. 6. View Synthesis Results with Different Positional Embedding Methods: The red-highlighted areas show zoomed-in regions of the synthesized views alongside their corresponding error maps. The standalone MLP demonstrates the poorest performance, exhibiting significant color inaccuracies and distortions in image features. In contrast, our proposed approach, combining normalization, positional encoding, and MLP (Norm+PosEnc+MLP), achieves the most accurate results, preserving both color fidelity and fine image details.

Qinbo Li and Nima Khademi Kalantari. 2020. Synthesizing Light Field from a Single Image with Variable MPI and Two Network Fusion. *ACM Trans. Graph.* 39 (11 2020), Issue 6. <https://doi.org/10.1145/3414685.3417785>

Kai-En Lin, Yen-Chen Lin, Wei-Sheng Lai, Tsung-Yi Lin, Yi-Chang Shih, and Ravi Ramamoorthi. 2023. Vision transformer for nerf-based view synthesis from a single input image. In *Proceedings of the IEEE/CVF Winter Conference on Applications of Computer Vision*. 806–815.

Minghua Liu, Chao Xu, Haian Jin, Linghao Chen, Mukund Varma T, Zexiang Xu, and Hao Su. 2024. One-2-3-45: Any single image to 3d mesh in 45 seconds without per-shape optimization. *Advances in Neural Information Processing Systems* 36 (2024).

Ruoshi Liu, Rundi Wu, Basile Van Hoorick, Pavel Tokmakov, Sergey Zakharov, and Carl Vondrick. 2023. Zero-1-to-3: Zero-shot one image to 3d object. In *Proceedings of the IEEE/CVF international conference on computer vision*. 9298–9309.

Ben Mildenhall, Pratul P. Srinivasan, Matthew Tancik, Jonathan T. Barron, Ravi Ramamoorthi, and Ren Ng. 2021. NeRF: Representing Scenes as Neural Radiance Fields for View Synthesis. *Commun. ACM* 65, 1 (dec 2021), 99–106. <https://doi.org/10.1145/3503250>

Thomas Müller, Alex Evans, Christoph Schied, and Alexander Keller. 2022. Instant neural graphics primitives with a multiresolution hash encoding. *ACM transactions on graphics (TOG)* 41, 4 (2022), 1–15.

Ryan S Overbeck, Daniel Erickson, Daniel Evangelakos, Matt Pharr, and Paul Debevec. 2018. A system for acquiring, processing, and rendering panoramic light field stills

for virtual reality. *ACM Transactions on Graphics (TOG)* 37, 6 (2018), 1–15.

Guo Pu, Peng-Shuai Wang, and Zhouhui Lian. 2023. SinMPI: Novel View Synthesis from a Single Image with Expanded Multiplane Images. In *SIGGRAPH Asia 2023 Conference Papers*. 1–10.

Abhilash Sunder Raj, Michael Lowney, Raj Shah, and Gordon Wetzstein. 2016. Stanford lytro light field archive.

Martin Rerabek and Touradj Ebrahimi. 2016. New light field image dataset. In *8th International Conference on Quality of Multimedia Experience (QoMEX)*.

Steven M Seitz and Charles R Dyer. 1999. Photorealistic scene reconstruction by voxel coloring. *International journal of computer vision* 35 (1999), 151–173.

Hamid R Sheikh and Alan C Bovik. 2006. Image information and visual quality. *IEEE Transactions on image processing* 15, 2 (2006), 430–444.

Pratul P Srinivasan, Tongzhou Wang, Ashwin Sreelal, Ravi Ramamoorthi, and Ren Ng. 2017. Learning to Synthesize a 4D RGBD Light Field From a Single Image. *Proceedings of the IEEE International Conference on Computer Vision (ICCV)*. https://openaccess.thecvf.com/content_iccv_2017/html/Srinivasan_Learning_to_Synthesize_ICCV_2017_paper.html

Richard Tucker and Noah Snavely. 2020. Single-view view synthesis with multiplane images. In *Proceedings of the IEEE/CVF Conference on Computer Vision and Pattern Recognition*. 551–560.

Zhou Wang, A.C. Bovik, H.R. Sheikh, and E.P. Simoncelli. 2004. Image quality assessment: from error visibility to structural similarity. *IEEE Transactions on Image Processing* 13, 4 (2004), 600–612. <https://doi.org/10.1109/TIP.2003.819861>

- Zhou Wang, Eero P Simoncelli, and Alan C Bovik. 2003. Multiscale structural similarity for image quality assessment. In *The Thirty-Seventh Asilomar Conference on Signals, Systems & Computers, 2003*, Vol. 2. Ieee, 1398–1402.
- Daniel Watson, William Chan, Ricardo Martin-Brualla, Jonathan Ho, Andrea Tagliasacchi, and Mohammad Norouzi. 2022. Novel view synthesis with diffusion models. *arXiv preprint arXiv:2210.04628* (2022).
- Alex Yu, Vickie Ye, Matthew Tancik, and Angjoo Kanazawa. 2021. pixelnerf: Neural radiance fields from one or few images. In *Proceedings of the IEEE/CVF conference on computer vision and pattern recognition*. 4578–4587.
- Emin Zeman, Manu Gond, Soheib Takhtardeshir, Roger Olsson, and Mårten Sjöström. 2024. A Spherical Light Field Database for Immersive Telecommunication and Telepresence Applications. In *2024 16th International Conference on Quality of Multimedia Experience (QoMEX)*. 200–206. <https://doi.org/10.1109/QoMEX61742.2024.10598264>
- Richard Zhang, Phillip Isola, Alexei A Efros, Eli Shechtman, and Oliver Wang. 2018. The Unreasonable Effectiveness of Deep Features as a Perceptual Metric. In *CVPR*.
- Hang Zhao, Orazio Gallo, Iuri Frosio, and Jan Kautz. 2016. Loss functions for image restoration with neural networks. *IEEE Transactions on computational imaging* 3, 1 (2016), 47–57.
- Tinghui Zhou, Richard Tucker, John Flynn, Graham Fyffe, and Noah Snavely. 2018. Stereo Magnification: Learning View Synthesis Using Multiplane Images. *ACM Trans. Graph.* 37, 4, Article 65 (jul 2018), 12 pages. <https://doi.org/10.1145/3197517.3201323>
- Wenhui Zhou, Gaomin Liu, Jiangwei Shi, Hua Zhang, and Guojun Dai. 2020. Depth-guided view synthesis for light field reconstruction from a single image. *Image and Vision Computing* 95 (2020), 103874. <https://doi.org/10.1016/j.imavis.2020.103874>
- Wenhui Zhou, Jiangwei Shi, Yongjie Hong, Lili Lin, and Ercan Engin Kuruoglu. 2021. Robust dense light field reconstruction from sparse noisy sampling. *Signal Processing* 186 (9 2021). <https://doi.org/10.1016/j.sigpro.2021.108121>